Numerical Modeling of Space Plasma Flows: ASTRONUM-2011
ASP Conference Series, Vol. 459
N. V. Pogorelov, J. A. Font, E. Audit, and G. P. Zank, eds.

Numerical Study of the Global Corona for CR 2055 Driven by Daily Updated Synoptic Magnetic Field

Xueshang Feng,[1] L. P. Yang,[1] C. Q. Xiang,[1] Yang Liu,[2] Xuepu Zhao,[2] and S. T. Wu[3]

[1]*SIGMA Weather Group, State Key Lab of Space Weather, Center for Space Science and Applied Research, Chinese Academy of Sciences, PO Box 8701, Beijing 100190, China*

[2]*W.W. Hansen Experimental Physics Laboratory, Stanford University, Stanford, CA 94305, USA*

[3]*Center for Space Plasma and Aeronomic Research, The University of Alabama in Huntsville, Huntsville, AL 35899, USA*

Abstract. In this paper, a preliminary study of the global corona for Carrington rotation (CR) 2055 is carried out by the 3D Solar-Interplanetary (SIP) adaptive mesh refinement (AMR) space-time conservation element and solution element (CESE) MHD model (SIP-AMR-CESE MHD model) (Feng et al. 2011a), which is driven by the daily-updated magnetic field synoptic data. To incorporate the observations into the model, the lower boundary conditions are specified according to the flux evolution of the observed magnetic field and the normal projected characteristic method. The simulated results are compared with solar observations and in-situ solar wind measurements, which are mapped from both Ulysses and other near-Earth spacecraft to the computation domain. Comparisons show that the MHD results have good overall agreement with coronal and interplanetary structures, including the size and distribution of coronal holes and the transition of the solar wind speeds and magnetic field polarities. The MHD results are also compared with the Potential Field Source Surface (PFSS) and Wang-Sheeley-Arge (WSA) methods.

1. Introduction

The solar coronal magnetic field is of great importance to determine the structure of the solar corona. Since direct measurements of the coronal magnetic field are not routinely available (Judge 1998; Lin et al. 2000; Petrie and Patrikeeva 2009), the global MHD model has become one of the most effective tools to extrapolate the coronal magnetic field and investigate the nature of the solar corona from photospheric magnetic field and other observations. Usually, researchers initialize the MHD codes for the global solar corona and solar wind by using potential magnetic field based on the synoptic charts of the magnetic field and Parker solar wind solution to obtain a steady-state equilibrium through the time relaxation method. To construct a synoptic chart, the daily photospheric magnetograms of the whole specified CR are used by overlaying them and a weighted average is employed for overlapping regions (Arge and Pizzo 2000). In these charts, the data at different Carrington longitudes are sampled at different time instances

and only those near central meridian from each magnetogram are adopted (Zhao, X. P., J. T. Hoeksema, and P. H. Scherrer, 2011, private communication). In addition, the constructed synoptic chart does not have sufficient information at the particular time in the specified CR. Therefore, it seems more reasonable to use the most recent observations when investigating a particular event (Hayashi et al. 2008).

A better choice will be to use the daily-updated magnetic field synoptic charts comprised by the most recent 360° of observations and beginning with the leading edge of the most recent magnetogram (Arge and Pizzo 2000). The daily-updated maps are much more sensitive to the quality of the individual magnetograms than the original synoptic charts. If MHD models can be driven by the most recent magnetic observations, they will be able to keep pace with the changes of the magnetic field configuration.

Considering these points, we will use daily-updated magnetic field synoptic data to drive the time-dependent MHD simulation, then present the preliminary simulated results of CR 2055 as a validation test. In Section 2, we will describe the model and the treatments of the solar surface boundary conditions. Section 3 will compare the simulation results with the daily and synoptic observations (constructed in the same way as producing the synoptic magnetic field chart), and the mapped in-situ measurements from Ulysses and OMNI data as done by Neugebauer et al. (1998) and Linker et al. (1999). The daily and the synoptic data come from the Extreme Ultraviolet Imagers (EUVI) and the white-light measurements of the inner coronagraph (COR1) onboard the spacecraft of the Solar Terrestrial Relations Observatory ahead of Earth (STEREO A). In addition, the polarized brightness (pB) observations from the Large Angle Solar COronagraph (LASCO) C2 onboard the Solar and Heliospheric Observatory (SOHO) are also used to check the MHD model. The last section is reserved for a brief summary.

2. The 3D SIP-AMR-CESE MHD Model

2.1. Model description

The basic equations governing the system are the set of the MHD equations in the conservative form in the frame corotating with the Sun. The details about the governing equation have been given in Feng et al. (2011a). Following Feng et al. (2010, 2011a), we have also added the similar source terms in the energy equation to mimic the distribution of the fast and slow solar winds. The calculation is carried out by SIP-AMR-CESE MHD model, which has been presented by Feng et al. (2007, 2010, 2011a). Here are given the basic concepts. To implement adaptive mesh refinement (AMR) of the SIP-CESE MHD model on the six-component grid system of the spherical shell domain, the governing MHD equations are transformed from the physical space (x, y, z) or (r, θ, ϕ) to the computational space (ξ, η, ζ) while retaining the form of conservation (Jiang et al. 2010; Feng et al. 2011a), and the SIP-AMR-CESE MHD model is implemented in the reference coordinates with the help of the parallel AMR package PARAMESH.

The computational region in this paper extends from 1 to 27 R_S. Initially, the computational domain is divided into $8 \times 4 \times 4$ blocks with each block consisting of $6 \times 6 \times 6$ cells, and the blocks near the Sun are refined to have two refinement levels. To start the computation, the Parker's hydrodynamic solar wind solution (Parker 1963) is used to give the initial values of the plasma density, ρ, gas pressure p, and the plasma

velocity **u**. Here, the initial temperature and number density on the solar surface are prescribed to be 1.3×10^6 K and 1.5×10^8 cm^{-3}, respectively. At the same time, the potential magnetic field based on the daily-updated magnetic field synoptic data of the first day in CR 2055 is calculated in the corona as our initial magnetic field input. Then, we integrate the MHD equations in time by relaxation until a converged steady-state equilibrium is achieved. In what follows, the solar wind solution is updated by the 3D SIP-AMR-CESE MHD, which employs the bottom boundary conditions presented in Section 2.2, and thus can capture the coronal responses to the surface magnetic field variations. During the calculation, a grid cell size of 0.015 R_S is achieved on the solar surface and at most five levels of grid refinement are obtained in the computational domain. The grid during the simulation is refined or derefined to obtain a grid cell size of ~ 0.21 R_S near the current sheet and a maximum grid cell size of ~ 2 R_S at the outer boundary.

2.2. Boundary Conditions

To investigate the coronal responses to the changing magnetic field measured on the solar surface, we input a sequence of daily-updated magnetic field synoptic charts, in which the magnetic fields change at a rate corresponding to real time. Since the cadence of the daily-updated synoptic maps is roughly about 24 hours, the magnetic field data on the solar surface are prepared by simply taking the difference of the two time sequences of the maps and then linearly increasing with time to drive the evolution. The radial magnetic field on the solar surface for new time step is given as

$$B_r(\theta,\phi)^{n+1} = B_r(\theta,\phi)^n + \triangle B_r(\theta,\phi)\triangle t \tag{1}$$

with

$$\triangle B_r(\theta,\phi) = \frac{(B_r(\theta,\phi))_{m+1} - (B_r(\theta,\phi))_m}{24 \times 3600} \tag{2}$$

where $\triangle t$ is the usual time step restricted by the Courant-Friedrichs-Lewy (CFL) condition, m denotes the mth daily-updated synoptic map and n is the nth time step.

When B_r varies with time, it is necessary to specify a non-zero tangential electric field $\mathbf{E}_t$ to make the flux evolve to match the observed changes of the magnetic field (Mikić et al. 1999). According to Song et al. (1999) and Mikić et al. (1999), when a time-varying B_r is taken into consideration, $\mathbf{E}_t$ can be prescribed by $\mathbf{E}_t = \nabla_t \times (\Psi \hat{e}_r)$, where Ψ is a function of θ and ϕ, and ∇_t indicates tangential derivative operator in the $\theta - \phi$ plane. Once we get $\frac{\partial \mathbf{B_r}}{\partial t}$ from Equation (2), Ψ can be determined by the Poisson equation $\nabla_t^2 \Psi = \frac{\partial \mathbf{B_r}}{\partial t}$, where ∇_t^2 is $\nabla_t \cdot \nabla_t$. From the ideal MHD condition

$$\mathbf{E}_t = -(\mathbf{u} \times \mathbf{B})_t \tag{3}$$

we can obtain two additional constraints of the bottom boundary conditions.

Besides the three constraints deduced from Equations (1) and (3), in order to specify the evolution of all the physical quantities, we need to determine another five bottom boundary conditions. These five constraints are defined with the help of the projected characteristics method along the radial direction (Wu et al. 2006; Hayashi 2005; Jiang et al. 2010; Feng et al. 2011a).

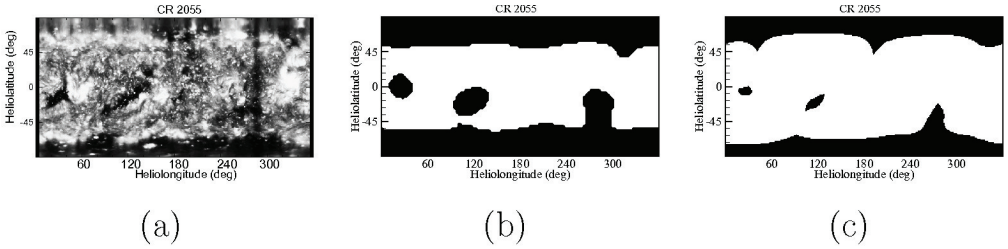

Figure 1. Synoptic maps of the coronal holes at 1 R_S in CR 2055. Panel *a* is the observation by STEREO-A EUVI 195 Å. Panels *b* and *c* are the simulated coronal holes, represented with the black color, from the MHD and PFSS models.

3. Numerical Results for CR 2055

3.1. Comparison with Disc Images

Coronal holes are believed to be associated with open magnetic field regions and to be the source regions of fast solar wind (de Toma 2010). They are typically identified as dark regions in ultraviolet (UV) and X-rays radiations by their low emission intensity due to the expansion of the solar wind. Figure 1 displays the synoptic maps of coronal holes at 1 R_S from the EUVI observations, SIP-AMR-CESE MHD model (hereafter called the MHD model for brief) and PFSS model in CR 2055. Figure 1 shows that there are two low-latitude holes centered at about $(\theta, \phi) = (-10°, 25°)$ and $(220°, -240°)$. In the simulated results, the former hole shifts towards the solar equator by 10°. Additionally, both the simulation and the observations reveal that the two polar coronal holes (PCHs) are roughly confined to 60° poleward. Figure 2 shows the synoptic maps of the plasma parameters for CR 2055. The typical simulated density at the base of the coronal hole is about 1×10^8 cm^{-3}, the temperature is 2×10^6 K and the radial speed is 2.5 km s^{-1}. Near the magnetic neutral lines, they are 2×10^8 cm^{-3}, 2.5×10^6 K and 0.5 km s^{-1}, respectively. These values are in good agreement with those derived from STEREO/EUVI observations (e.g., Frazin et al. (2009); Vásquez et al. (2010)). Therefore, basically speaking, the simulation has captured the shapes and distributions of the coronal holes and generated reasonable distributions of the plasma parameters due to the proper inner boundary treatments. In addition, the coronal holes obtained by the PFSS model are not as pronounced as the simulated holes.

3.2. Comparison with Synoptic pB Images and Daily Observations

Figure 3 presents the synoptic white-light polarized brightness (pB) maps at 2.5 R_S for CR 2055. From this figure, we can see that the locations of the current sheet calculated from both the MHD and PFSS models are roughly consistent with those of the bright white-light structures at the east and west limbs. The brightest structures are coincident with the locations where the latitudes of the current sheet vary least with longitude. In addition, a pronounced 4-sector structure of the current sheet, i.e., a rough double sinusoid, is located between the latitudes of ±30° both in the observation and in the simulation at 2.5 R_S, which indicates that there is a strong quadrupole component in the photospheric field. During CR 2055, the HCSs from both the MHD and PFSS models have almost the same shape and location, while the HCS from the MHD model deflects more abruptly, compared with that from the PFSS model. Figure 3 also displays that the locations of the brightest structures in the white-light pB images at the east and

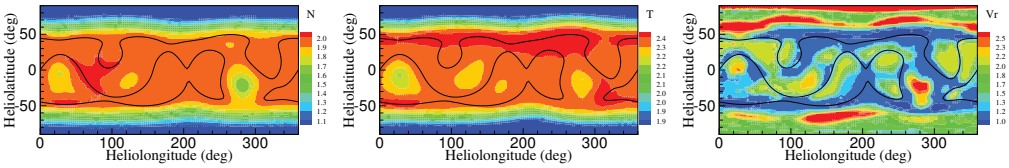

Figure 2. Synoptic maps of the simulated number density N in units of 10^8 cm^{-3}, temperature T in units of 10^6 K, and radial speed v_r in units of km s^{-1} at 1 R_S for CR 2055, where the black lines denote the magnetic neutral lines.

west limbs are characterized by the lowest velocity and highest plasma density in the simulation, and the dark regions are coincident with the locations of the high-speed and low-density flow. Therefore, the MHD model has reproduced the observed large contrasts in the number density and radial speed between open and closed field regions.

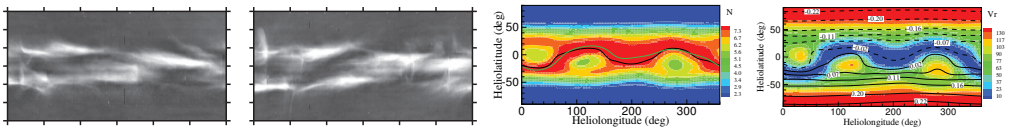

Figure 3. Synoptic maps at 2.5 R_S for CR 2055. Panels *a* and *b* are the white-light pB images at the east and west limbs from SOHO LASCO C2 or STEREO-A COR1. Panel *c* is the simulated number density N in units of 10^5 cm^{-3}, where the black line denotes the magnetic neutral line from the MHD model and the green line from the PFSS model. Panel *d* overlays the isolines of the radial magnetic field in units of Gauss on the contour map of the simulated radial speed v_r in units of km s^{-1}.

Figure 4 presents the daily observations and the simulated results corresponding to Day 13 of CR 2055. Figures 4 shows that the bright, thin streamers are restricted to a narrow range of lower latitudes and the higher latitudes are dominated by the large, dark polar coronal holes. The bright long "jets" above 3 R_S at the east and west limbs seem a little wider in the simulation results. These jets result from the emission of the classic helmet streamers close to the sky plane. In addition, there are also diffusive and less bright radial structures outside 3 R_S. From the Mark-IV coronagraph observation and the simulated results in Figures 3 and 4, we find that these diffusive structures result from the projection effects of the high-density structures off the plane of sky, which are associated with a single, warped current sheet encircling the Sun.

3.3. Comparison with Interplanetary Measurements

In order to test the simulated results at both high and low heliographic latitudes, we compare the MHD model predictions with the mapped observations from both Ulysses and OMNI, just as done by Mikić et al. (1999) and Linker et al. (1999). At the same time, the WSA model (McGregor et al. 2011) is also employed to check our MHD model. Figure 5 displays the synoptic images at 20 R_S for CR 2055. In this figure, the mapped points are plotted versus heliographic latitude and Carrington longitude, with the Ulysses' observations shown in black-line bounded regions and the OMNI data in white-line bounded regions. In Panels (a) and (b), the red regions show the fast-speed solar wind, and the blue regions the slow-speed solar wind. Whereas, in Panel

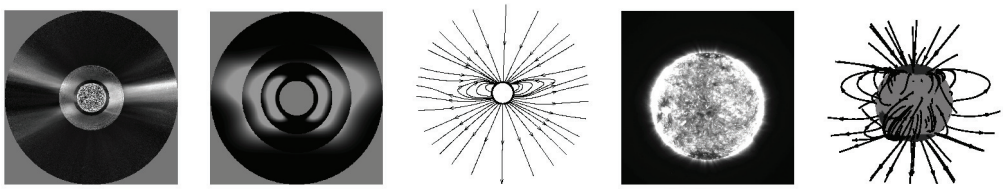

(a) (b) (c) (d) (e)

Figure 4. The coronal observations and simulated results in the meridional plane at $\phi = 180°$ and $0°$ for CR 2055. Panels *a* and *b* are the pB images obtained by the coronal composite observations and the MHD results from 1.15 to 6 R_S, respectively. In Panel *a*, the data from 1.15 to 2.3 R_S come from Mauna Loa Solar Observatory (MLSO) Mark-IV coronameter and the observation from 2.3 to 6 R_S is from LASCO C2. Panel *c* displays the magnetic field topological structures projected in this meridional plane from 1 to 6 R_S, and Panel *d* is the observation on the solar disk from the STEREO-A EUVI 195 Å for the same day as the coronal composite image in Panel *a*. Panel *e* is the simulated 3D magnetic field lines from 1 to 2 R_S with open-field regions shown in black color and closed-field regions in gray color.

(c), the red regions represent the negative polarities and the blue regions the positive polarities. As shown in Figure 5, both the MHD simulation and the WSA model have well reproduced Ulysses' observations of the solar wind speed and the magnetic field polarities, the MHD model gives a relatively wider coverage of low-speed solar wind than the modified WSA model. Roughly speaking, the sector structures of the magnetic field predicted by the MHD model seem closer to the observation than that from the PFSS model. Furthermore, the sector structures from the PFSS model are much more uniform than those from both the observation and the MHD model.

Both the simulated results and the mapped near-Earth measurements demonstrate that the low-latitude regions are not dominated by the low-speed solar wind as was during the previous two minima (Tokumaru et al. 2010), but interrupted by two broad intermediate or fast streams during this CR, although their peak values (~ 600 km s^{-1}) are somewhat lower than the flow speed of the common fast polar streams in the previous solar minimum. In addition, the phasings of the fast streams predicted by both the MHD and the WSA models are offset by less than two days from the observations.

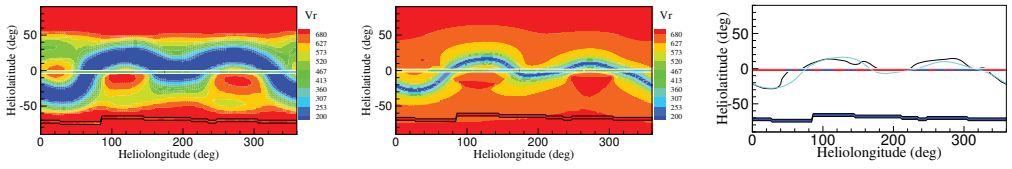

(a) (b) (c)

Figure 5. Synoptic images at 20 R_S of the mapped interplanetary measurements for CR 2055. Panel *a* is the simulated radial speed v_r in units of km s^{-1}. Panel *b* is the predicted radial speed from the WSA model (McGregor et al. 2011). Panel *c* presents the observed magnetic polarities and the magnetic neutral lines (MNLs), where black and the azure lines denote the MNLs from the MHD and the PFSS results.

4. Summary and Discussion

Here, a 3D SIP-AMR-CESE MHD model (Feng et al. 2011a) is utilized to simulate the dynamic evolution of the global solar corona for CR 2055 driven by the daily-updated magnetic field synoptic data. In the model, the combination of the tangential component of the electric field at the bottom boundary and the method of projected characteristics is employed to specify the bottom boundary conditions. The advantage that the MHD model can keep pace with the variation of the photospheric magnetic field enables us to reproduce some observations. Comparisons with the solar observations and the mapped interplanetary measurements show that the time-dependent MHD model can capture the features of both solar corona and solar wind.

Despite the fact that our time-dependent MHD model has partially succeeded in reproducing the observations, there are still many problems to be solved, such as data deficiency in the photospheric magnetic field measurements and coronal heating in the numerical model. Furthermore, to incorporate additional continuous solar observations will lead to the more realistic data-driven, time-dependent solar wind model.

Acknowledgments. The work is jointly supported by the National Natural Science Foundation of China (41031066, 40921063, 40890162, and 41074122), 973 program 2012CB825601 and the Specialized Research Fund for State Key Laboratories. The numerical calculation has been completed on our SIGMA Cluster computing system. STW is supported by NSF ATM-0754378, NSF 0132798 via AURA SubAward C10569A, and NASA EPSCoR NNX09AP74A.

References

Arge, C. N., and Pizzo, V. J., 2000 J. Geophys. Res., 105, 10,465.
de Toma, G., 2010 Solar Phys., 272, 213–226.
Feng, X., Zhou, Y. and Wu, S. T., 2007 ApJ, 655, 1110–1126.
Feng, X., Yang, L., Xiang C., Wu S. T., Zhou Y., and Zhong D., 2010 ApJ, 723, 30.
Feng, X. S., Yang L. P., Xiang, C. Q. , Jiang, C. W., Ma, X. P., Wu, S. T., Zhong, D. K., and Zhou, Y. F. , 2011a Solar Phys., in press.
Feng, X., Zhang, S., Xiang, C., Yang, L., Jiang, C., and Wu, S. T. , 2011b ApJ, 734, 50.
Frazin, R. A., Vásquez, A. M., and Kamalabadi, F., 2009 ApJ, 701, 5470.
Hayashi, K., 2005, ApJ, 161, 480.
Hayashi, K., Zhao, X. P., and Liu, Y., 2008 J. Geophys. Res., 113, A07,104.
Jiang, C., Feng X., Zhang J., and Zhong D., 2010 Solar Phys., 267, 463.
Judge, P. G., 1998 ApJ, 500, 1009.
Lin, H., Penn, M. J., and Tomczyk, S., 2000 ApJ, 541, L83.
Linker, J. A., et al., 1999 J. Geophys. Res., 104, 9809.
McGregor, S. L., Hughes, W. J., Arge, C. N., Owens, M. J., and Odstrcil, D., 2011 J. Geophys. Res., 116, A03,101.
Mikić, Z., Linker, J. A., Schnack, D. D., Lionello, R., and Tarditi, A., 1999 Phys. Plasma , 6, 2217.
Neugebauer, M., et al., 1998 J. Geophys. Res., 103, 14587.
Parker, E. N., 1963 Interplanetary dynamical processes. (New York: Interscience Publ. Inc.)
Petrie, G. J. D., and Patrikeeva, I., 2009 ApJ, 699, 8714.
Song, W. M., Zhang, X. J., Wang, Y., and Ren,X. Y., 1999 Chin. J. Radio Sci., 14.
Tokumaru, M., Kojima, M., and Fujiki, K., 2010 J. Geophys. Res., 115, A04,102.
Vásquez, A. M., Frazin, R. A., and Manchester, IV, W. B., 2010 ApJ, 715, 1352.
Wang, Y.-M., Sheeley, N. R., and Andrews, M. D., 2002 J. Geophys. Res., 107, 1465.
Wu, S. T.,Wang, A. H., Liu, Y., and Hoeksema, J. T., 2006 ApJ, 652, 800.